Applied Catalysis B: Environmental 140–141 (2013) 213–224

Contents lists available at SciVerse ScienceDirect

Applied Catalysis B: Environmental

journal homepage: www.elsevier.com/locate/apcatb

Microwave-assisted synthesis of (S)Fe/TiO_2 systems: Effects of synthesis conditions and dopant concentration on photoactivity

K. Esquivel[a,b,*], R. Nava[b], A. Zamudio-Méndez[b], M. Vega González[c], O.E. Jaime-Acuña[d], L. Escobar-Alarcón[e], J.M. Peralta-Hernández[a], B. Pawelec[f], J.L.G. Fierro[f,**]

[a] Centro de Innovación Aplicada en Tecnologías Competitivas, Omega 201, Fracc. Delta, C.P. 37545 León, Mexico
[b] Facultad de Ingeniería, UAQ, Cerro de las Campanas, C.P. 76000 Santiago de Querétaro, Qro., Mexico
[c] Centro de Geociencias, UNAM, Blvd. Juriquilla 3001, C.P. 76230 Santiago de Querétaro, Qro., Mexico
[d] Centro de Investigación Científica y de Educación Superior de Ensenada, Ensenada, B.C., Mexico
[e] Departamento de Física, ININ, Carr. México-Toluca, C.P. 52750 Ocoyoacac, Edo., Mexico
[f] ICP-CSIC, Cantoblanco, 28049 Madrid, Spain

ARTICLE INFO

Article history:
Received 4 January 2013
Received in revised form 21 March 2013
Accepted 27 March 2013
Available online xxx

Keywords:
Microwave photocatalysis
Fe/TiO_2
S/TiO_2
X-ray diffraction
Photodegradation
Methyl red

ABSTRACT

TiO_2 and Fe(S)-doped TiO_2 photocatalysts have been synthetized by a microwave-assisted method and deeply characterized by means of several techniques (N_2 adsorption–desorption isotherms, scanning electron microscopy (SEM), TEM, high resolution transmission electron microscopy (HRTEM), powder X-ray diffraction (XRD), temperature-programmed desorption of NH_3 (TPD-NH_3) and UV–vis diffuse reflectance, Raman and XPS spectroscopic techniques). The synthetized samples were tested in the photodegradation of methyl red dye under UV irradiation at room temperature. Depending on the temperature and duration of the microwave synthesis, some changes in the textural and crystalline structure of the titanium dioxide were observed which influenced on the photocatalytic activity. The best photocatalyst found in this study was the one doped with S (0.1 wt.%) prepared by microwave-assisted synthesis at 215 °C for 60 min and calcined at 550 °C. The enhancement of color removal over this sample (49% of color removal) was associated to the formation of anatase phase and the enhancement of the sample acidity with respect to undoped TiO_2 sample. A volcano-shaped curve was obtained for methyl red degradation against TiO_2 crystal size. Catalyst calcination at 700 °C led to a drastic drop in activity due to formation of large TiO_2 crystals of rutile phase, as confirmed by XRD.

1. Introduction

Titanium dioxide has been widely used and investigated owing to its relatively low cost, oxidizing power, nontoxicity and photostability [1]. Since the report on the photocatalytic splitting of water using rutile TiO_2 electrodes in 1972, the interest in titanium dioxide as strategic material for environmental processes has increased. These processes are mainly related to photocatalysis, photovoltaic devices and dye-sensitized solar cells [2–4].

Each application of the titania requires a specific crystalline structure, morphology, surface area and, usually, a specific size [3]. Among the TiO_2 crystalline structures (anatase, brookite and rutile), the anatase and rutile exhibit photocatalytic activity under UV illumination, but its applications are still limited due to its negligible photoactivity when irradiated with visible light [4]. Thus, attempts to extend the TiO_2 light absorption into the visible region to improve the photocatalytic activity have been made by substitution of Ti^{4+} in the TiO_2 lattice by metal ion modification, such as Fe, Ni, Co, Au, Ag, Cr, Sn, La, Ce, Zr, Mn, W and B [1,5–19], and by nonmetal doping with N [20–26], F [26], C [27,28] and S [29–35], where the substitution occurs in the oxygen vacancy (anionic doping). In both of these approaches, impurity/defect states were introduced into the band gap of TiO_2, which lead to TiO_2 being able to absorb visible light [22,34,35]. In particular, the introduction of defects through selective doping of TiO_2 with Fe^{3+} has been demonstrated to be an effective method to diminish electron–hole recombination rate and/or to influence on interfacial electron-transfer rates [6]. However, the catalytic role of Fe^{3+} as dopant still remains controversial. On one hand, it is believed that Fe^{3+} cations can act as shallow traps in the titania lattice [36]. On the other hand, their role in decreasing the reduction of electron–hole recombination

* Corresponding author at: Centro de Innovación Aplicada en Tecnologías Competitivas, Omega 201, Fracc. Delta, C.P. 37545 León, México.
Tel.: +52 442 192 12 00x65427.
** Corresponding author. Tel.: +34 91 585 4769.
E-mail addresses: karen.esquivel@uaq.mx (K. Esquivel), jlgfierro@icp.csic.es (J.L.G. Fierro).
URLs: http://www.uaq.mx (K. Esquivel), http://www.icp.csic.es/eqsgroup/ (J.L.G. Fierro).

0926-3373/$ – see front matter © 2013 Elsevier B.V. All rights reserved.
http://dx.doi.org/10.1016/j.apcatb.2013.03.047

rate is still unclear [7,36]. As compared to the iron doping [5–8 and references within], the photoefficiency of the S-doped TiO_2 systems is much less studied [29–36]. This is probably because depending on the catalyst preparation method employed the cationic [29,32,33] or anionic substitution might occur [30,31]. In this sense, density functional theory (DFT) calculations allowed conclude that the substitution of S at the O sites of TiO_2 (anion doping) could be chemically favored under Ti-rich conditions while Ti^{4+} ions substitution by S (cation-doping) could be favored under O-rich conditions [30]. Interestingly, it was reported that the S cation-doped TiO_2 photocatalysts showed stronger visible light absorption than the S anion-doped counterparts [32]. In case of the substitution of S at the O sites of TiO_2, the modification of the electronic structures of TiO_2 leading to the band gap narrowing was observed [29] or it was proposed that S^{2-} ions might act as deep hole traps that diminish the oxidizing power of the hole [31].

A number of methods have been used to prepare and modify TiO_2 nanoparticles, such as sol–gel method [8], chemical vapor deposition [37], solvothermal process [38], sputtering [39,40], reverse micelle method [41], liquid phase deposition [42], electrochemical method [14] and hydrothermal treatment [16,43]. Among them, the sol–gel has been the most widely methodology employed. In recent years, microwave irradiation method has received considerable attention as a new promising method for the preparation of nanomaterials with controlled shape and size [3,44–51]. The main advantage of microwave irradiation is that it offers a simple, rapid, and economical strategy of heating. Compared with conventional heating, microwave heating has advantages for chemical synthesis, for example, the microwave energy is introduced without direct contact between the energy source and the reacting chemicals and this process can lead to much higher heating rates and in certain way it can realize selective heating, also other advantages are the reduction of reaction time by orders of magnitude, higher uniformity in the product and better properties when compared to conventional heating methods [22,23,45,52–63]. Thus, the microwave synthesis method has opened up the possibility of realizing new reactions in a very short time and wide applications in the synthesis of organic and inorganic materials, although it is still less explored in inorganic material synthesis [64].

In the present study, Fe/TiO_2 and S/TiO_2 were prepared by the sol–gel method and then microwave heated at different temperature and reaction times to observe the effect of the microwave in the textural characteristics, crystalline phase and photocatalytic activity of the resultant material. Nevertheless, there are plenty literature works dealing with the effect of the Fe^{3+} and S^{2-} ions in the TiO_2, however, to the best of our knowledge, so far no investigation is presented using the sol–gel microwave assisted method. Detailed characterization of the morphology (S_{BET}, SEM, TEM) and structure (X-ray diffraction, XPS, UV–vis DRS and Raman) of these systems is reported together with their performance for the photocatalytic degradation of methyl red (MR) dye under UV light irradiation. Analysis of the results allowed us to establish a relationship between the photocatalytic activity and the textural, structural and electronic characteristics of the Fe- and S-doped TiO_2 photocatalysts.

2. Experimental

2.1. Microwave-assisted synthesis of TiO_2-based photocatalysts

The synthesis of the TiO_2 substrate was obtained by slowly dissolving the titanium precursor (titanium isopropoxide, 97% Aldrich, TTIP) in an organic solvent (isopropanol, 99.9%, J.T. Baker), the titanium solution was continuously magnetically stirred for 20 min under nitrogen atmosphere. The hydrolysis process was then performed by adding water into the flask containing precursor/solvent mixture and magnetically stirred for 1 h [65]. The molar ratio of the precursors and solvents are, 0.03:4.2:1 for TTIP:H_2O:isopropanol, respectively. For the Fe-modified TiO_2 samples, the iron precursor was $FeSO_4{\cdot}7H_2O$ (J.T. Baker), and for the S-loaded TiO_2 samples, the precursor was thiourea (NH_2CSNH_2, J.T. Baker). These precursors were added separately by dissolving them into the water used for the hydrolysis reaction in different weight percentage (0.005, 0.01 and 0.1 wt.%). The obtained sol was transferred into Teflon-lined vessels and placed on a turn table for uniform heating using a microwave reaction system (Synthos 3000, Anton Paar). The change in temperature in the reaction vessel was monitored automatically by the dual-IR temperature probe and the solutions were continuously stirred at medium speed (300 rpm). The heating procedures were conducted for 30 min at 180 °C and 215 °C, and for 60 min at 215 °C using microwave radiation of 600 W, and finally the system was cooled down to room temperature. The obtained powder was filtered and washed with deionized water several times and room temperature dried for 18 h and subsequently dried at 80 °C for 20 h in a conventional furnace. A calcination process was carried out at 450, 550 and 700 °C by 3 h to improve the sample crystallinity. For the sake of ease understanding, Fig. 1 summarizes the steps followed in the synthesis of samples calcined at 450 °C. The Fe- and S-doped samples will be labeled hereafter as xFe/TiO_2 and xS/TiO_2 where x is nominal wt% of the dopant element. Due to the overlapping of Y band (reference element) with that of Ti (324 nm) and the very low metal loading (0.005 wt.%), chemical analysis of samples cannot be performed by ICP-AES technique. Thus, metal loadings in this work refer to the nominal ones.

2.2. Photocatalyst characterization

Surface morphology analysis of the materials was carried out by Scanning Electron Microscopy (SEM) with a microscope JEOL JSM-6060 LV. The accelerating voltage employed was 15 kV. Elemental analysis was performed by Energy Dispersive X-ray Spectroscopy (EDS) (EDS Oxford Inca X-Sight coupled to a MT 1000, Hitachi). Also the morphology analysis was carried out by high resolution transmission electronic microscopy (HRTEM) using a JEOL JEM 2000FX microscope. The catalysts were crushed and dispersed ultrasonically in acetone at room temperature and then spread onto a perforated carbon–copper microgrid. The operational accelerating voltage was 200 kV using a filament of LaB_6. Bandgap energy (E_{bg}) values were determined from diffuse reflectance measurements (Cary 5000 UV-Vis-NIR Varian spectrophotometer) by applying the Kubelka–Munk function, F(R), and the method proposed by Tandon and Gupta [66], according to which E_{bg} corresponds to the point where the linear increase of the Kubelka–Munk function starts. The nitrogen adsorption–desorption isotherms were recorded using an Autosorb iQ2 equipment. The specific surface area and the pore size distribution were calculated by applying the BET equation to the nitrogen adsorption isotherm and the Barret–Joyner–Halender (BJH) method to desorption branch of the nitrogen isotherm, respectively. X-ray diffraction analysis (XRD) were obtained using a Bruker D8 advanced diffractometer equipped with a Cu seal tube to generate Cu K_α radiation ($\lambda = 1.5406$ A) within the Bragg angles $10 < 2\theta < 80^\circ$ in steps of 0.01°. Raman spectroscopy was used to identify the nature of titania phases. Details of measurements are provided in SI. Surface analysis of samples was carried by X-ray photoelectron spectra (VG Escalab 200 R spectrometer equipped with a hemispherical electron analyser and a Mg Kα ($h\nu = 1253.6$ eV) X-ray source). For the sake of saving printed space, details of the experimental measurements are given in SI. The acidity of the samples was determined by

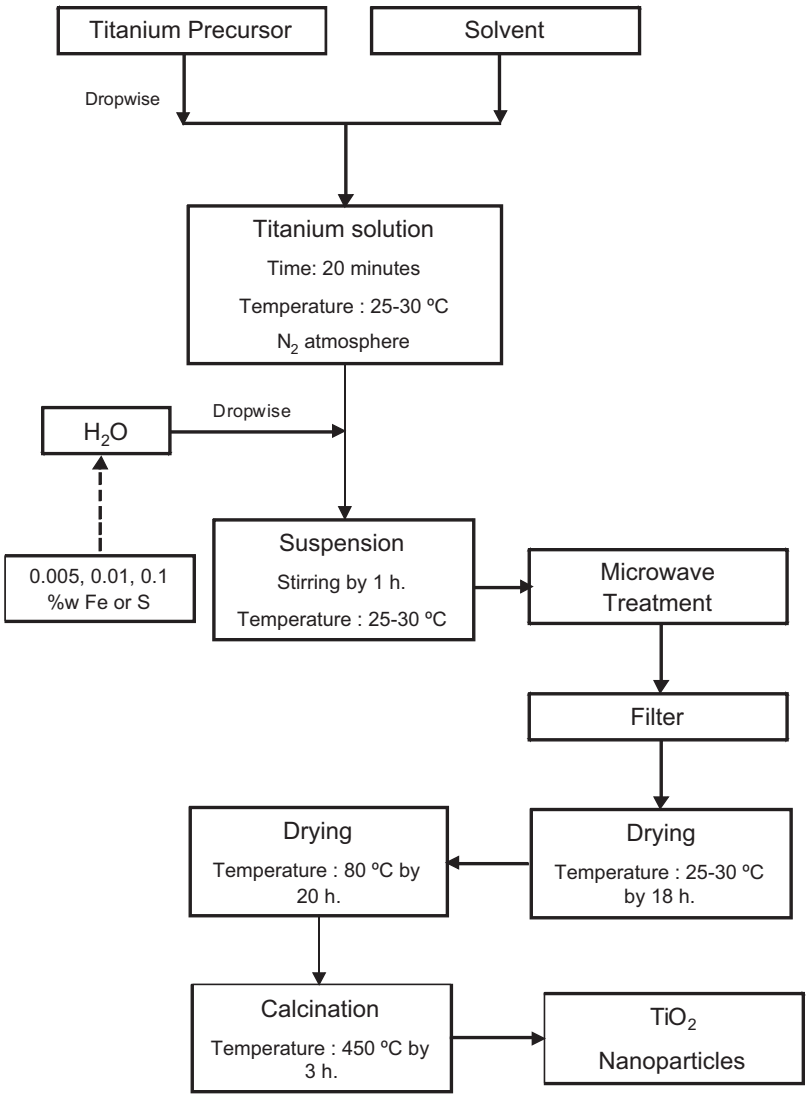

Fig. 1. Flow chart for preparation of samples via microwave radiation and calcination at 450 °.

temperature-programmed desorption (TPD) of ammonia measurements conducted on a Micromeritics 2900 equipment provided with a TCD and interfaced to a data station. Sample (0.050 g) pretreated in a He (383 K for 1 h) was ammonia-saturated in a stream of 5% NH_3/He (Air Liquide) flow (50 mL min^{-1}) at 100 °C for 1 h. Ammonia was desorbed using a linear heating rate of 15 °C min^{-1} from r.t. to 550 °C.

2.3. Photocatalytic experiments

The photocatalytic activity of the synthetized samples was evaluated in the photodegradation reaction of methyl red (MR) dye (2-(N,N-dimethyl-4-aminophenyl)azobenzene carboxylic acid, Sigma-Aldrich) using a solution of 25 mg L^{-1} at pH = 5. In each test, 50 mg of the photocatalyst was dispersed in 100 mL of the dye solution bubbled with air and magnetically stirred for 30 min in the darkness before irradiation. The system was illuminated using two UV lamps (GE, λ = 365 nm and P = 15 W cm^{-2}). At given irradiation time intervals and after 3 h of total reaction time, the samples (2 mL) were taken out and the color removal was monitored by UV–vis absorption at λ = 429 nm (the *azo* bond), which is frequently employed method for the preliminary catalyst screening [5,67]. The samples were centrifuged (Universal 320 Hettich Zentrifugen) for 20 min at 5500 rpm before analysis. Residual methyl red (MR) in solution was calculated according to the following equation:

$$\text{residual MR} = \left[\frac{A_0/A_t}{A_0}\right] \times 100\% \quad (1)$$

where A_0 is initial absorbance of the band centered at 429 nm and A_t is the absorbance of MR at reaction time of 3 h.

3. Results

3.1. Photocatalyst characterization

3.1.1. Textural properties

The specific surface area and average pore diameters of the TiO_2, xFe/TiO_2 and xS/TiO_2 (x = 0.005, 0.01 and 0.1 wt.%) are listed in Table 1. About the textural properties for the un-doped sample (TiO_2), the results show that the surface area (S_{BET}) decreases according the increase in the temperature and reaction time in the microwave system. Also the S_{BET} values decrease after the calcination process and a notable change is appreciate when the synthesis condition is at 180 °C for 30 min a decrease of 56% in the S_{BET} value is observed but when the synthesis condition is of 215 °C by 60 min, the decrease in the S_{BET} value is only of 39%. The pore diameter

Table 1
Textural properties[a] and band gap values[b] of the TiO_2-based photocatalysts.

Material	Microwave synthesis conditions	E_{bg} (eV)		Surface area ($m^2\ g^{-1}$)		Pore diameter (nm)	
		Dried	Calc. 450 °C	Dried	Calc. 450 °C	Dried	Calc. 450 °C
TiO_2	180 °C/30 min	3.15	3.15	233	101	4.3	6.6
	215 °C/30 min	3.13	3.12	213	91	4.9	6.6
	215 °C/60 min	3.1	3.12	182	110	6.6	6.6
0.005Fe/TiO_2	180 °C/30 min	3.13	3.10	229	108	4.3	5.6
	215 °C/30 min	3.16	3.10	210	–	4.9	–
	215 °C/60 min	3.11	3.10	196	–	4.9	–
0.01Fe/TiO_2	180 °C/30 min	3.13	3.10	227	–	4.3	–
	215 °C/30 min	3.12	3.10	210	–	5.6	–
	215 °C/60 min	3.12	3.10	204	114	6.6	6.6
0.1Fe/TiO_2	180 °C/30 min	3.15	3.10	236	–	4.3	–
	215 °C/30 min	3.18	3.10	220	–	4.9	–
	215 °C/60 min	3.15	3.10	208	–	4.9	–
0.005S/TiO_2	180 °C/30 min	3.15	3.10	225	–	4.9	–
	215 °C/30 min	3.14	3.10	179	–	4.3	–
	215 °C/60 min	3.10	3.10	194	–	4.9	–
0.01S/TiO_2	180 °C/30 min	3.15	3.10	232	–	4.3	–
	215 °C/30 min	3.13	3.10	–	–	–	–
	215 °C/60 min	3.10	3.12	201	112	4.9	6.6
0.1S/TiO_2	180 °C/30 min	3.15	3.11	224	–	4.3	–
	215 °C/30 min	3.13	3.10	–	123	–	6.6
	215 °C/60 min	3.10	3.10	–	119	–	6.6

[a] As determined by N_2 adsorption–desorption isotherms at −196 °C.
[b] E_{bg}: band gap as determined by UV–vis DRS by applying the Kubelka–Munk function, F(R), and the method proposed by Tandon and Gupta [66], according to which E_{bg} corresponds to the point where the linear increase of the Kubelka–Munk function starts

of the dried samples ranges from 4.3 to 6.6 nm by increasing the temperature and reaction time. After the calcination process, in all cases the pore diameter is 6.6 nm.

In the *x*Fe/TiO_2 samples, the S_{BET} values also decrease by increasing the temperature and reaction time, however the values are higher than the TiO_2 by increasing the iron weight percentage (0.005, 0.01 and 0.1) at 215 °C by 30 and 60 min of reaction time. This effect was presented and studied in previous reports [68]. Also as in the pure TiO_2, the S_{BET} values decrease after the calcination process although a change is appreciated independent of the Fe weight percentage used when the synthesis condition is at 180 °C for 30 min a decrease of 53% in the S_{BET} value is observed but in the case of when the synthesis condition is of 215 °C for 60 min, the decrease in the S_{BET} value is only of 44%. By analyzing the results of the effect of the Fe on the textural properties of the dried *x*Fe/TiO_2 samples, it appears that Fe limits the temperature effect and improves the S_{BET} of the TiO_2. The pore diameter for all cases and before the calcination process is around 4.9 nm and it changes to 6.6 nm as the un-doped TiO_2.

For the S-doped TiO_2, the S_{BET} values also decrease by increasing the temperature and reaction time as was discussed with the un-doped and Fe-doped TiO_2. The S_{BET} values are higher than the TiO_2 by increasing the sulfur weight percentage (0.005, 0.01 and 0.1) at 215 °C by 30 and 60 min of reaction time. After the thermal treatment, the S_{BET} values present the same tendency of decreasing as in the previous samples.

3.1.2. Morphological and structural analysis (SEM and HRTEM)

In Fig. 2 is presented the SEM micrographs for the un-doped, Fe- and S-doped TiO_2. The surface appearance in all cases (in all dopant weight percentage used) is formed by similar rhombohedra geometry with different particle sizes and dispersed in a non-homogeneous way. It is not possible to observe a remarkable difference in morphology between the TiO_2 and the doped samples. By the EDS analysis the only elements detected were the Ti and O, no presence of Fe and S was observed. This could be attributed to the small amount of the dopant added to the synthesis.

In Fig. 3(a) is presented the TEM analysis in scale of 50 nm showing for the un-doped TiO_2 a particle size around of 25 nm, also it is possible to observe that the clusters are formed by sintering of the crystallites and that the boundary between grains is less obvious than in the sample synthesized by the usual sol-gel method (micrographs are not shown). In the case of the 0.1 wt% S-doped sample (Fig. 3(b)), the shape of the crystallites is similar. Fig. 3(c) shows a HRTEM image of the 0.1S/TiO_2 sample in scale of 10 nm. The HRTEM image of this sample shows the crystalline TiO_2 nanoparticles having mainly spherical shape. The spacing between the two adjacent lattice planes (about 0.315 nm) matches with the *d* value reported for TiO_2 [1 0 1] face [69]. The fact that the particle consists of pure TiO_2 was confirmed by EDS. The grain size of TiO_2 particles in anatase phase is about 11 nm. Although the presence of S species in the 0.1S/TiO_2 photocatalyst was confirmed by EDS, the HRTEM did not show S particles probably due to a very low S loading (0.1 wt%) as well as the limitation of this technique for visualizing average sample composition.

3.1.3. Band gap measurements

UV–vis DRS technique was used to study the influence of synthesis conditions on the band gap (E_{bg}) of the synthetized samples. The band gap energies estimated from the UV–vis absorption spectra are listed in Table 1. The band gap of the pure TiO_2 decreases according the synthesis conditions; it shows that at higher temperature and longer reaction time the band gap changes from 3.15 to 3.10 eV. After the calcination process the bang gap value remains constant, at the synthesis condition of 180 °C for 30 min of reaction time (3.15 eV) and it changes to 3.12 eV at 215 °C for 30 and 60 min of reaction time, respectively. These values are in good agreement to the literature (3.10–3.20 eV for anatase phase) [9,68]. In the case of the Fe-doped samples, the band gap values are in the range between 3.11 and 3.18 eV, and by changing the synthesis conditions no remarkable change is appreciated upon the

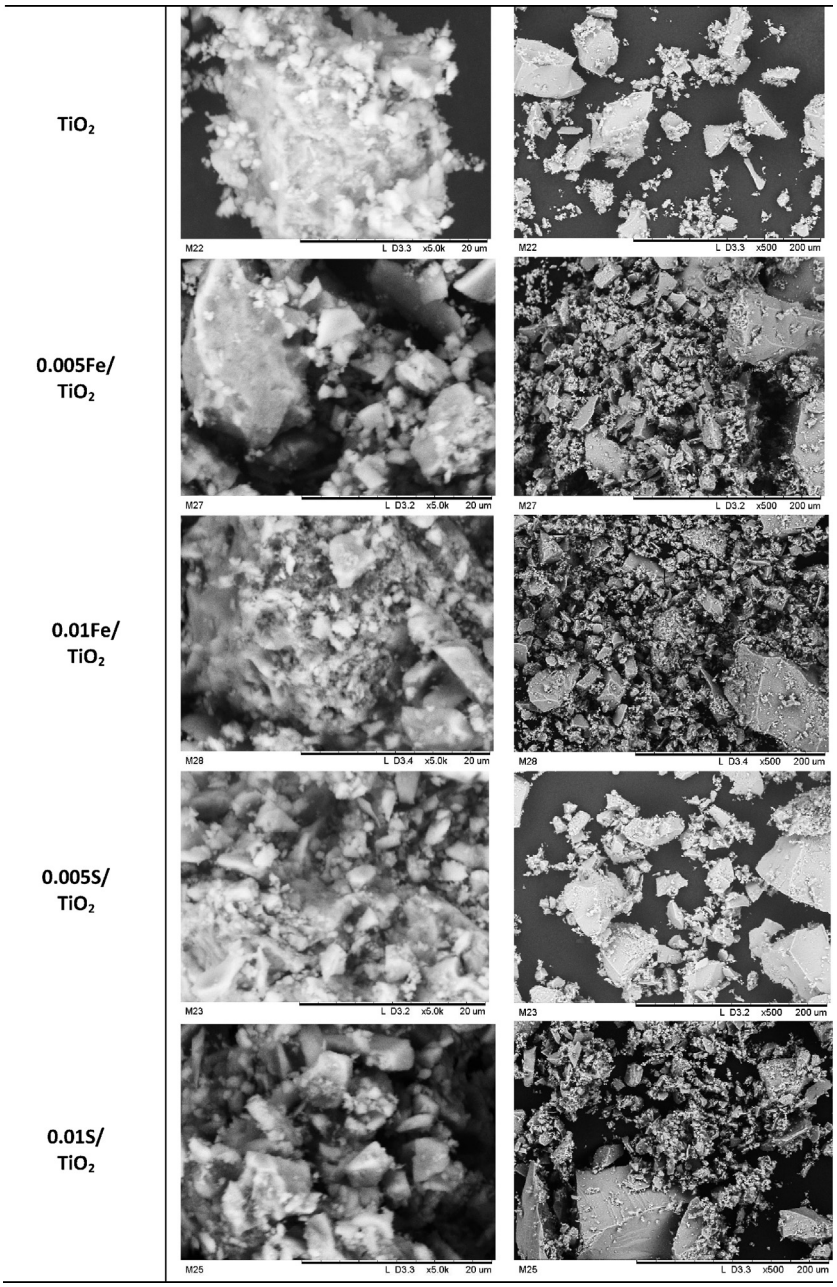

Fig. 2. SEM micrographs for the undoped, and Fe- and S-doped TiO_2.

iron weight percentage is increased (0.005–0.1 wt.%). In all cases after the calcination process the band gap is modified to 3.10 eV.

For the S-doped TiO_2, the band gap values are between 3.15 and 3.10 eV, at 180 °C for 30 min of reaction time and 215 °C for 60 min of reaction time, respectively, showing a decrease in the values according the temperature and reaction time increase and approaches the value recorded for pure TiO_2. These values remain in the same range no matter the change in the wt.% S incorporated during the synthesis. Finally, after the thermal treatment at 450 °C by 3 h the band gap values are adjust to 3.10 eV as in the Fe-doped samples.

3.1.4. X-ray diffraction (XRD)

Wide-angle XRD diffraction patterns were recorded to study the influence of synthesis conditions on the formation of any crystalline species in the TiO_2, xFe/TiO_2 and xS/TiO_2 samples. XRD patterns of un-doped TiO_2 are shown in Fig. 4(a). By changing the synthesis conditions and with the further thermal treatment, it is possible to see how the sample is getting ordered. The diffraction peaks detected in 2θ (25.4°, 37.8°, 48.1°, 53.9°, 55.2°, 62.8°, 68.6°, 70.3°, 75.1°) at the different synthesis conditions and after the calcination process indicates the presence of the crystalline anatase phase (JCPDS no.: 00-004-0477) [69]. From the diffraction pattern peak intensity, a preferential orientation of the plane (1 0 1) can be proposed. No diffraction signal appears showing the rutile phase. For the xFe/TiO_2 and xS/TiO_2 samples (Figs. 4(b) and (b), respectively), the effect of the calcination temperature is the same as in the case of the pure TiO_2, the anatase phase is getting ordered by the thermal process and no presence of rutile phase is detected as well no signal can be attributed to other crystalline phase of iron oxide or sulfur compounds. As it was mentioned, no presence of rutile phase was observed in any of the tested materials, that is why, the fraction of anatase X_A, is considered to be 1 [13,70].

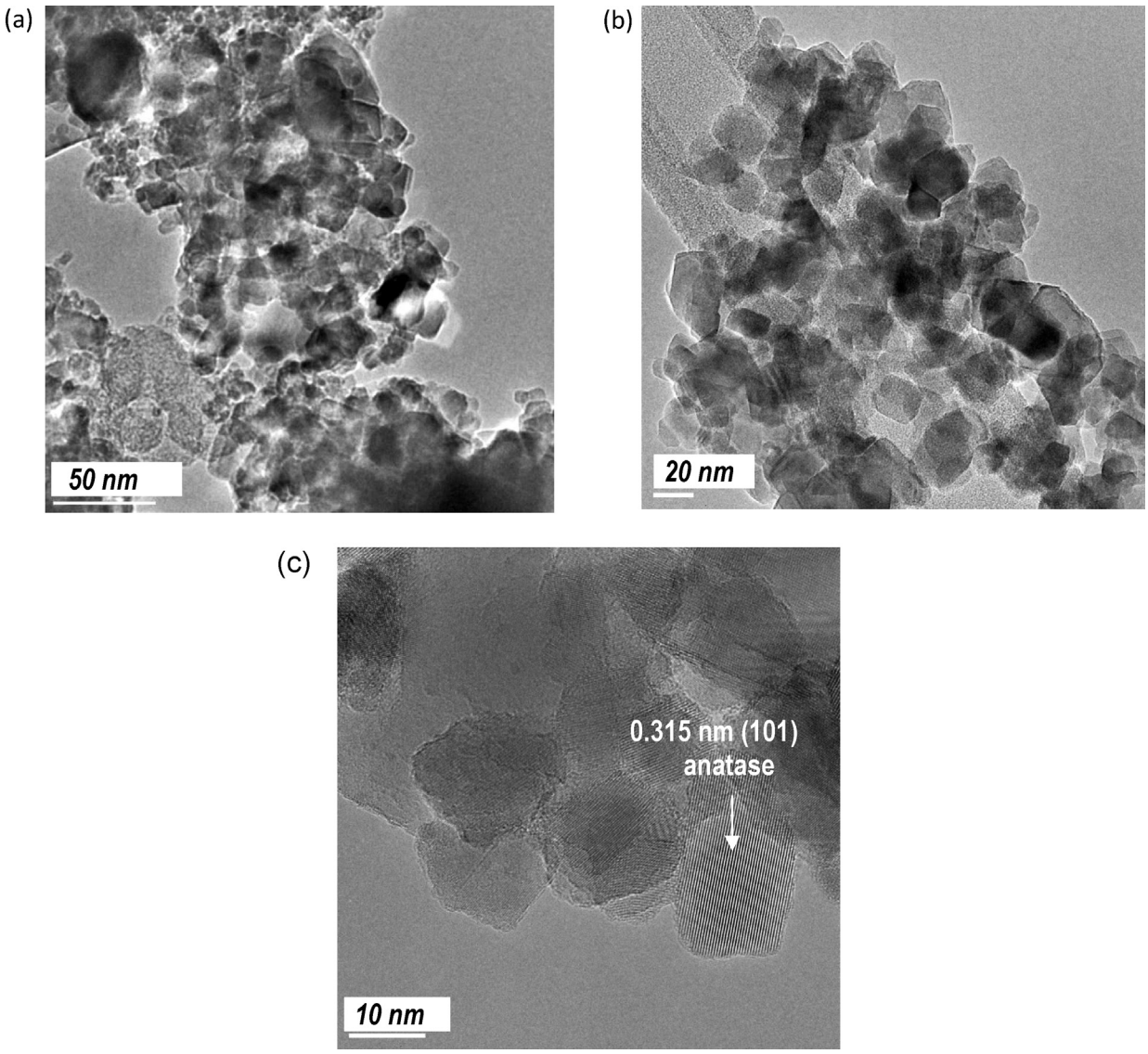

Fig. 3. TEM images of undoped TiO_2 (a) and 0.1S/TiO_2 (b) and (c) samples.

The crystallite sizes were calculated by the Debye–Scherrer equation and they are compiled in Table 2. For the un-modified TiO_2, the crystal size increases from 5.7 to 6.7 nm by changing the time and temperature of the synthesis procedure. After the calcination process these values increases to 9.7 nm (almost twice its size), however by increasing the time (60 min) and temperature (215 °C) at the synthesis procedure the crystal size only increases to a value of 8.9 nm (see Table 2). In the case of the Fe-loaded TiO_2 samples, the effect is the same. For example, for the 0.005Fe/TiO_2 sample calcined at 450 °C, an increase of temperature from 180 to 215 °C led to a small increase of the crystal size from 9.1 to 10.2 °C, however further increase of reaction time resulted in a decrease of crystal size to 8.5. About the S-doped TiO_2, the crystal size is slightly smaller than the TiO_2 and *x*Fe/TiO_2 samples, the values before the calcination processes are between 4.9 and 6.5 nm. By modifying the time to 60 min and temperature at 215 °C in the synthesis procedure the crystal size changes from 10.2 to 8.0 nm. In a representative way, to explore the calcination temperature on the crystal size, some of the materials were calcined at 550 °C and 700 °C showing that the crystal size increases more than twice its size as compared with the samples thermally processed at 450 °C (Table 2). It is emphasized here that microwave assisted synthesis favors the formation of crystalline anatase at temperatures substantially lower than that needed by conventional calcination.

Considering the crystal size of the samples prepared under the same synthesis conditions and calcination temperature (Table 2), it appears that the *x*S/TiO_2 and *x*Fe/TiO_2 samples show similar or even somewhat smaller crystal than the parent TiO_2 sample. For example, after calcination at 450 °C, TiO_2, 0.01Fe/TiO_2 and 0.1S/TiO_2 samples prepared at 180 °C for 30 min show similar crystallite sizes of 9.7, 9.4, and 9.4 nm, respectively. Thus, the changes in crystal sizes are very small, if any, for doped samples with very low loading as the ones employed in this study.

3.1.5. Raman spectroscopy

The crystal phase of the TiO_2, 0.01Fe/TiO_2 and 0.005S/TiO_2 photocatalysts was also confirmed with micro-Raman spectroscopy (Figs. 5 and 6). Using this technique it was possible to observe that dried TiO_2 sample shows only four typical lines corresponding to anatase phase, 147(E_g), 401(B_{1g}), 516(A_{1g}) and 640(E_g) cm^{-1} (Fig. 5(a)), having good agreement with those reported for the anatase phase [9]. After the sample calcination at 450 °C for 3 h, a new signal at 195(E_g) cm^{-1} appears and the other signals are better defined (Fig. 5(b)). In addition, dried TiO_2

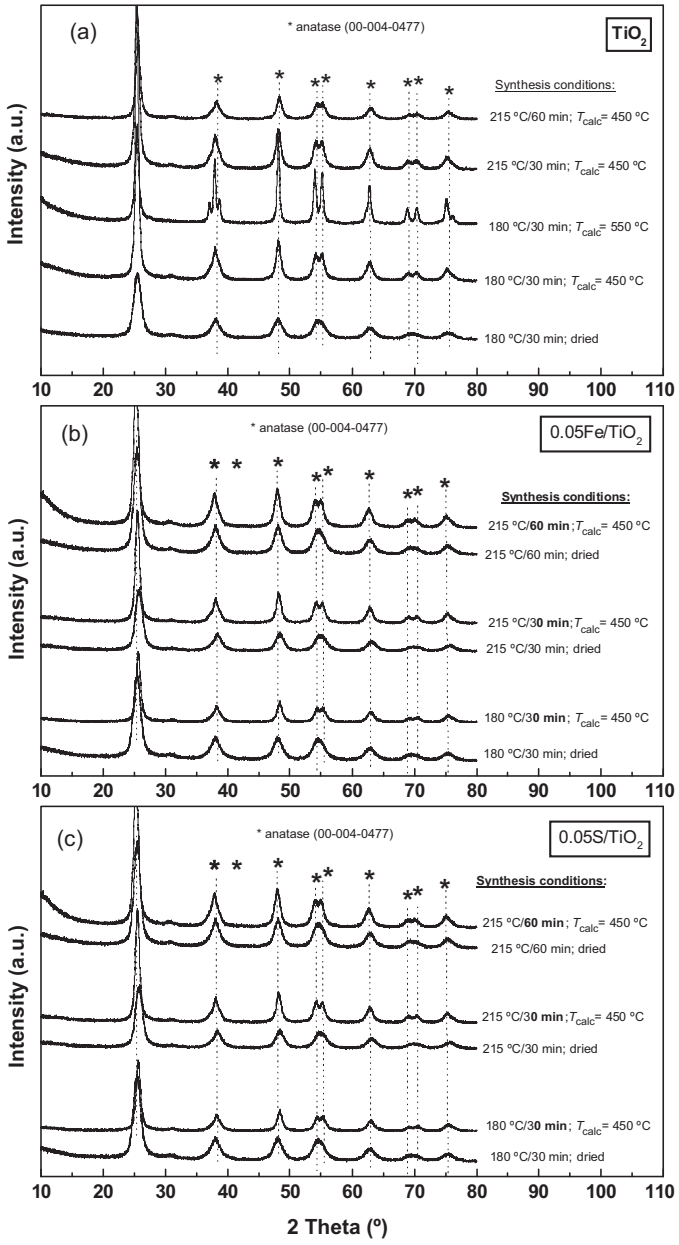

Fig. 4. XRD diffraction patterns of synthetized TiO_2 (a), $0.05Fe/TiO_2$ (b) and $0.05S/TiO_2$ (c) photocatalysts.

sample shows a shift of the 147(E_g) signal to lower values suggesting that the arrangement of the crystalline structure is taking place by changing the synthesis parameters (see inset of Fig. 5(a)) [13,68,71]. In the case of the Fe- and S-doped samples at the different amounts of dopant used, the same effect is presented (Fig. 6(a) and (b), respectively): after the thermal process at 450 °C, the missing signal at 195(E_g) cm^{-1} appears and a shift of the 147(E_g) cm^{-1} signal to lower values also is observed as in the un-doped TiO_2 samples. No presence of the rutile phase is detected as was observed in the XRD results, too. Finally, the comparison of Raman bands position of TiO_2, $0.01Fe/TiO_2$ and $0.1S/TiO_2$ samples prepared under the same synthesis conditions (Figs. 5 and 6) does not show any shift in the bands upon TiO_2 doping with small amounts of S and Fe dopants (0.005–0.1 wt.%).

3.1.6. Surface characterization by XPS

Wide survey scans (300–1300 eV) were recorded for all samples. Peaks belonging to Ti2p, O1s, O_{KLL} (Auger) and C1s (contamination) were clearly distinguished. Then high resolution O1s, Ti2p and S2p and Fe2p were recorded at 20 eV pass energy of the analyzer were scanned. All samples displayed O1s and Ti2p peaks with high intensity but S2p and Fe2p were only detected on the surface in $0.1S/TiO_2$ and $0.1Fe/TiO_2$ samples, respectively (see SI).

For the fresh $0.1S/TiO_2$ sample, a very weak S2p line at a binding energy of 168.9 ± 0.2 eV, which is characteristic of S(VI) species [72] was detected, however it moved to a binding energy of 162.1 ± 0.2 eV upon Ar^+ sputtering. As this energy belongs to sulfide species (S^{2-}), it can be inferred that sulfide is oxidized on the surface layer to sulfate during the synthesis. Considering the previous study by Hebenstreit et al. [73], the S2p peak at 162.1 ± 0.2 eV might well account for the presence of S^{2-} ions in the bulk which are resistant toward oxidation along the calcination step. Similar results were previously reported by Rockafellow et al. [31] and Miyauchi [72] for Ar^+ sputtered S-doped TiO_2 samples.

The $0.1Fe/TiO_2$ sample showed a very weak $Fe2p_{3/2}$ line at ca. 710.8 ± 0.2 eV, suggesting that iron remains as γ-Fe_2O_3 domains [74] but not as Fe^{3+} ions at titanium substitution sites in the lattice. This peak remained unchanged for both fresh and Ar^+-sputtered samples. It is also emphasized that S^{2-} and Fe^{3+} ions are highly dispersed within the bulk as concluded from the experimental $S/Ti = 0.0021 \pm 0.0002$ and $Fe/Ti = 0.0018 \pm 0.0002$ atomic ratios, respectively, which are rather close to the theoretical value ($M/Ti = 0.0025$) expected for a perfect, homogeneous distribution of S^{2-} and Fe^{3+} ions within the bulk TiO_2.

Fig. 7 displays the O1s core-level spectra of TiO_2, $0.1S/TiO_2$ and $0.1Fe/TiO_2$ samples synthetized at 215 °C for 60 min and calcined at 450 °C. As all O1s lines are asymmetric toward the high binding energy side, they were fitted to two components: a major one at 529.9–530.0 eV due to Ti—O—Ti bonds and a minor one at 531.1–531.3 eV associated to surface hydroxyl groups [75,76]. The ratio of the area of the component placed at high binding energy (hydroxyl groups) and total area of the O1s line gives the OH/O_{total} percentage on the surface of the samples. The OH/O_{total} values are

Table 2
Influence of the sample synthesis conditions and calcination temperature on the crystal size as determined by XRD data.

Material	Microwave synthesis conditions	Crystal size (nm)			
		Dried samples	Calcined		
			450 °C	550 °C	700 °C
TiO_2	180 °C/30 min	5.7	9.7	–	–
	215 °C/30 min	6.1	9.5	20.2	39.3
	215 °C/60 min	6.7	8.9	–	–
$0.005Fe/TiO_2$	180 °C/30 min	5.5	9.1	–	–
	215 °C/30 min	5.9	10.2	–	–
	215 °C/60 min	6.0	8.7	–	–
$0.01Fe/TiO_2$	180 °C/30 min	5.8	9.2	–	–
	215 °C/30 min	6.0	9.8	18.4	45.9
	215 °C/60 min	6.4	8.5	–	–
$0.1Fe/TiO_2$	180 °C/30 min	5.7	9.4	–	–
	215 °C/30 min	6.1	9.1	–	–
	215 °C/60 min	6.0	9.3	–	–
$0.005S/TiO_2$	180 °C/30 min	4.9	9.7	–	–
	215 °C/30 min	6.1	10.2	–	–
	215 °C/60 min	6.3	8.3	18.8	37.6
$0.01S/TiO_2$	180 °C/30 min	5.8	9.8	–	–
	215 °C/30 min	5.9	9.6	–	–
	215 °C/60 min	6.2	8.5	–	–
$0.1S/TiO_2$	180 °C/30 min	5.4	9.4	–	–
	215 °C/30 min	6.0	8.0	–	–
	215 °C/60 min	6.5	8.0	19.2	35.0

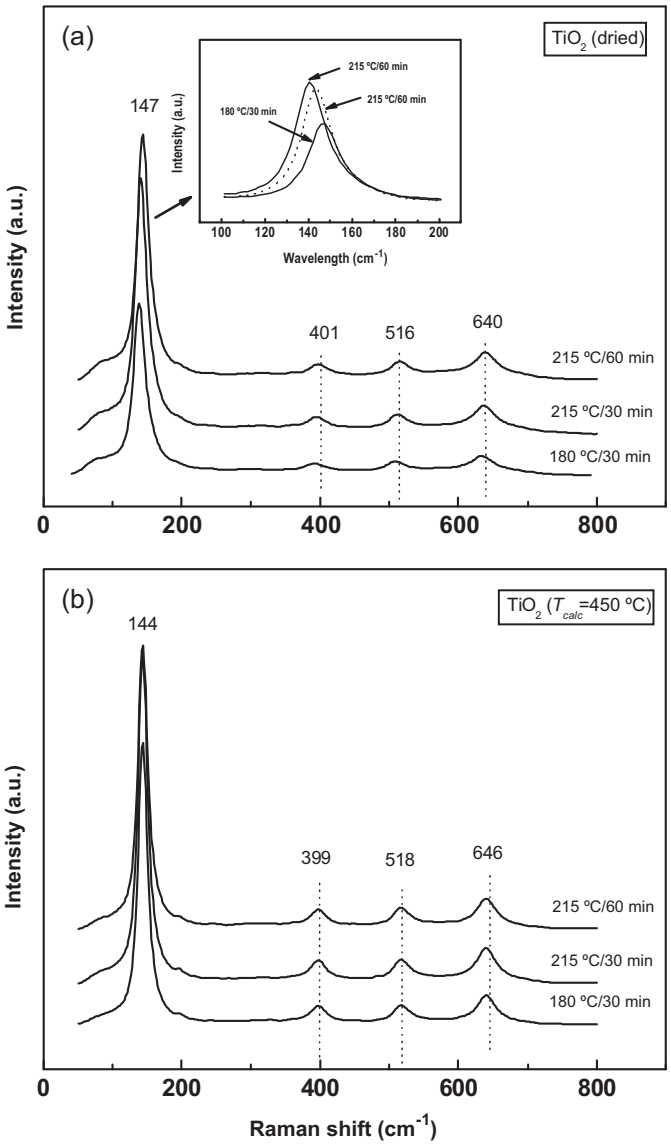

Fig. 5. Raman spectra of TiO_2 sample synthetized at different microwave conditions after drying (a) and calcination at 450 °C (b).

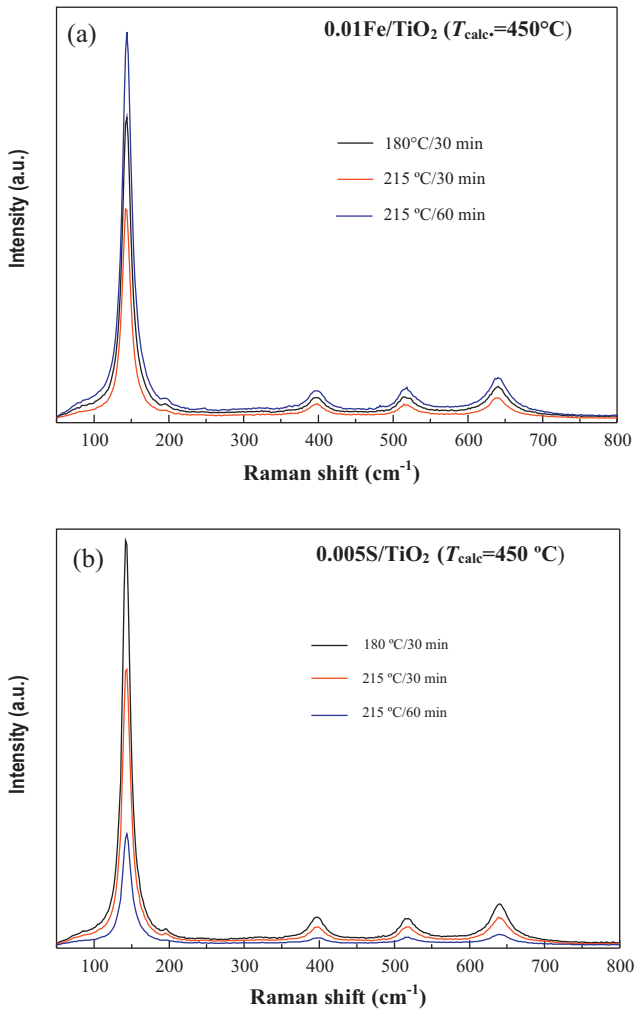

Fig. 6. Raman spectra of 0.01Fe/TiO_2 (a) and 0.005S/TiO_2 (b) samples after calcination at 450 °C.

0.10, 0.13 and 0.15 for TiO_2, 0.1Fe/TiO_2 and 0.1S/TiO_2 samples, respectively (estimated error in this calculation is 11%). A larger acidity of 0.1S/TiO_2 sample with respect to pure TiO_2 substrate was confirmed also by means of TPD-NH_3 technique (see inset of Fig. 10).

3.2. Methyl red photodegradation

To optimize the catalyst synthesis conditions, the efficiency of 21 photocatalysts was compared by evaluating the percentage of MR decoloration in aqueous solution. For all synthesized photocatalysts the percentage of MR decoloration at a reaction time of 3 h is compared in Fig. 8. From these data it is clear that photoactivity is determined by the synthesis conditions and calcination temperature on TiO_2-based samples. The TiO_2 calcined at 550 °C with the synthesis conditions for 30 min at 215 °C shows a high photocatalytic activity according to the rest calcination temperatures and synthesis conditions, removing near of 44% after 3 h of reaction time. Comparing this result with the *x*Fe/TiO_2 samples, it is possible to observe that the incorporation of the Fe(II) ion to the titanium dioxide by the microwave assisted synthesis does not show any improvement in the photocatalytic activity even when the samples is calcined at 550 °C. These results are still under interpretation of what can be causing the low catalyst efficiency. It is worth to mention that all the powder samples were calcined at different temperatures because no photoactivity was presented by using the dried samples having anatase phase.

By comparing these results with the *x*S/TiO_2 materials, the performance is improved when 0.005S/TiO_2 and 0.1S/TiO_2 samples are calcined at 550 °C. With these photocatalysts is possible to achieve a similar color removal (42%) in the case of the 0.005 wt.% of S (42%) compared with the pure TiO_2 (thermally treated at 550 °C) and a higher color removal with 0.1 wt.% of sulfur, reaching 49%. This result could be associated to the change in the textural properties such as the surface area, crystal size and the time of the microwave irradiance over the material. Considering the percentage of the color removal on the samples calcined at 550 °C (Fig. 8), the most effective photocatalysts were: 0.1S/TiO_2 (215 °C for 60 min) > TiO_2 (215 °C for 30 min) ≈ 0.005S/TiO_2 (215 °C for 60 min). This trend is discussed below on the basis of the catalyst activity–structure relationship and by comparing the pseudo-first order reaction rate constants for the most optimized catalysts.

In order to assess the effect of the initial concentration of the dye on the kinetics of color disappearance, different concentrations of initial methyl red solutions were tested (5, 10, 25, 40 and 50 mg L^{-1}). These experiments were performed using 0.1 wt.% of S as a doping agent since this proportion showed the best results in

Table 3
Influence of the initial methyl red concentration in solution on the kinetics of color disappearance[a] on TiO_2 and $0.1S/TiO_2$ photocatalysts.

Concentration ($mg\,L^{-1}$)	k_{obs} (min^{-1})	R^2	k_c ($mg\,L^{-1}\,min^{-1}$)	R^2	K_{MR} ($(mg\,L^{-1})^{-1}$)
TiO_2					
5	0.0095	0.945			
10	0.0036	0.961			
25	0.0021	0.966	0.015	0.950	0.191
40	0.0005	0.941			
50	0.0003	0.945			
$0.1S/TiO_2$					
5	0.0232	0.991			
10	0.0141	0.988			
25	0.0040	0.996	0.114	0.96	14.167
40	0.0030	0.975			
50	0.0003	0.982			

[a] k_{obs}: pseudo-first order rate constant calculated from Eq. (2); k_c, rate constant, K_{MR}: Langmuir–Hinshelwood adsorption equilibrium constant.

the degradation tests previously carried out. The obtained values of k_{obs} ranged between 0.0095 and 0.0003 min^{-1} for the pure TiO_2 and between 0.0232 and 0.0003 min^{-1} for the S doped TiO_2 (see Table 3). As can be observed from the data obtained, in all cases the rate constant (k_{obs}) decreases as the initial dye concentration of the solution is increased. This observation can be explained using the Langmuir–Hinshelwood model (L–H model) [77,78], according to which the relationship between the degradation rate (r) and the concentration of the dye [MR] can be expressed as follows (Eqs. (2) and (3)) [77]:

$$r = k_c \frac{K_{MR}[MR]}{1 + K_{MR}[MR]_0} = k_{obs}[MR] \quad (2)$$

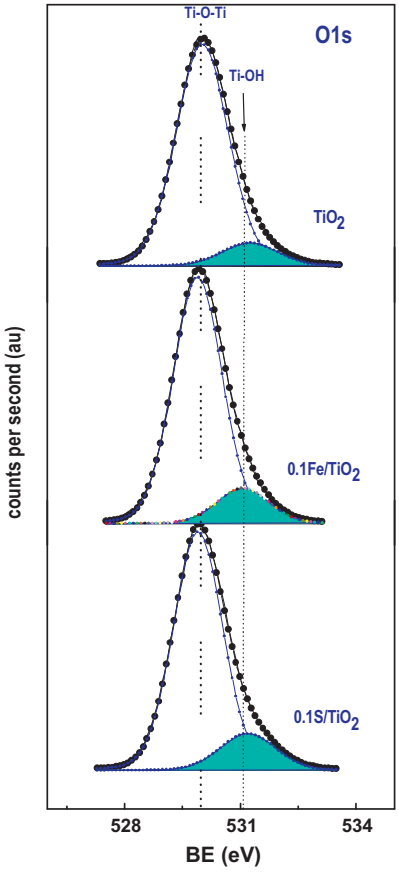

Fig. 7. O1s core-level XPS spectra of TiO_2, $0.1Fe/TiO_2$ and $0.1S/TiO_2$ samples synthetized at 215 °C for 60 min and then calcined at 450 °C.

$$\frac{1}{k_{obs}} = \frac{1}{k_c K_{MR}} + \frac{[MR]_0}{k_c} \quad (3)$$

where K_{MR} is the Langmuir–Hinshelwood adsorption equilibrium constant, k_c is the rate constant at the catalyst surface and k_{obs} is the pseudo-first order rate constant.

Fig. 9 shows that a plot of $1/k_{obs}$ versus $[MR]_0$ (Eq. (2)) results in a linear relationship. Calculating the value of K_{MR} from the intercept and k_c from the slope of the fitted straight line, it can be realized that the presence of the dopant enhances the surface rate constants, k_c, when it is compared to the un-doped TiO_2 (Table 3). In the case of $0.1S/TiO_2$ sample the rate is enhanced from 0.015 (TiO_2) to 0.114 $mg\,L^{-1}\,min^{-1}$. Also, K_{MR} is higher for the $0.1S/TiO_2$ sample [14.167 $(mg\,L^{-1})^{-1}$] than for the pure TiO_2 [0.191 $(mg\,L^{-1})^{-1}$]. The data treated using this model suggests that the dye reacts quickly on the surface of the doped semiconductor samples, thus inhibiting the blocking of the active sites of the semiconductor surface as occurs on the un-doped TiO_2.

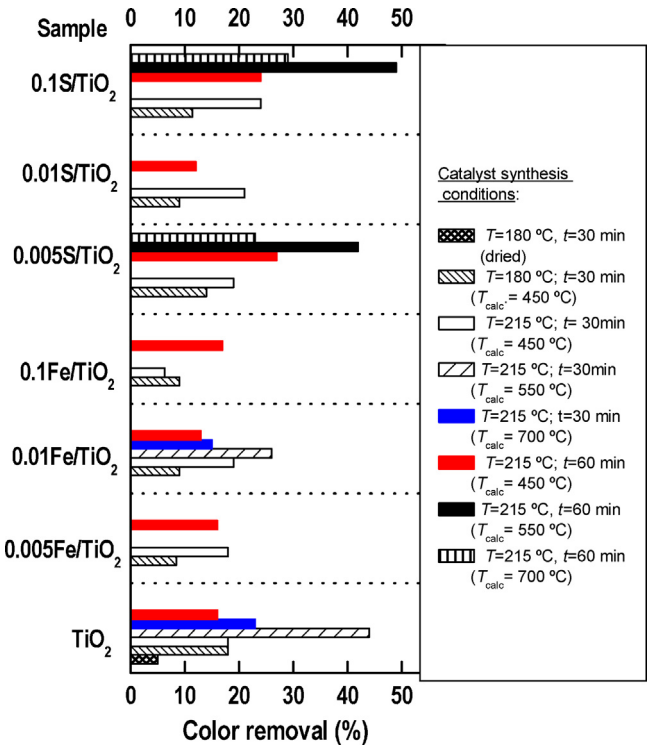

Fig. 8. Photodegradation under UV irradiation of methyl red dye for 3 h. Influence of the synthesis conditions and calcination temperature on the photoactivity of TiO_2-based systems.

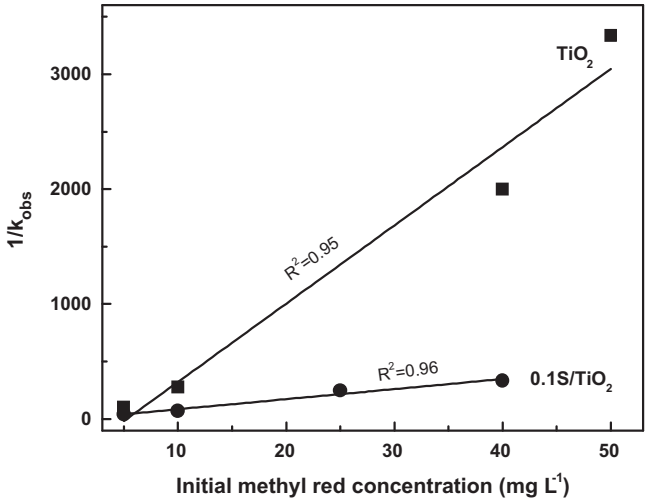

Fig. 9. Plot of $1/k_{obs}$ versus $[MR]_0$ (from Eq. (2)).

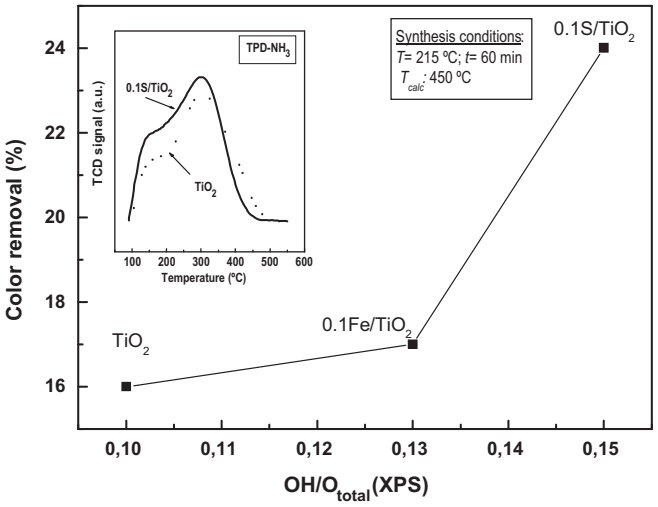

Fig. 10. Influence of the sample acidity (from XPS) on the color removal. Inset shown TPD-NH_3 patterns of the TiO_2 and 0.1S/TiO_2 samples synthetized at 215 °C for 60 min and then calcined at 550 °C.

4. Discussion

The effective role of dopants depends on several factors such as concentration, dispersion within the particles, electronic configuration and the energy level of the dopants with the TiO_2 lattice [7]. For the Fe-doped samples, the XPS results suggest that iron remains as γ-Fe_2O_3 domains but not as Fe^{3+} ions at titanium substitution sites in the lattice. On the contrary, for the S-doped samples, it is likely that S^{2-} incorporates into the oxide lattice even though it became oxidized and segregated as a sulfate phase during calcination. Therefore we consider that these S species and sulfate (or even OH groups) segregated at the grain boundaries may contribute the reduction of electron–hole recombination rate.

Considering the possible changes in the energy level of the dopants, this work demonstrated that microwave synthesis of Fe and S-doped TiO_2 samples at 180 °C for 30 min followed by calcination at 450 °C does not change to a significant extent the band gap with respect to undoped TiO_2 counterpart prepared under the same conditions (3.12–3.10 eV). Thus, the electronic factor does not explain the enhancement of MR decoloriorization on the 0.1S/TiO_2 with respect to its undoped TiO_2 counterpart. Moreover, regardless of the synthesis conditions, all photocatalysts did not show the less active rutile phase, as confirmed by XRD and Raman spectroscopy. The transformation of anatase into rutile phase with increasing the concentration of dopants was observed for much higher loadings than the ones used in this work [79].

It is commonly accepted that the mechanism of photocatalysis with semiconductors involves the formation of hydroxyl radicals ($^{\bullet}OH$) via two possible pathways: (i) when the valence band holes (h^+), which are photogenerated upon band gap photoextitation, oxidize H_2O, OH^- ions and/or the catalyst terminal —OH groups; and (ii) if molecular oxygen scavenges the electrons (e^-) photogenerated in the conduction band [80,81]. Thus, the catalyst efficiency could be accounted by considering the different proportion of OH groups available on the catalyst surface. The data in Fig. 10, strongly suggest that the population of hydroxyl groups as measured by the OH/O_{total} ratio (XPS) is a parameter that influences on the activity for color removal. This trend could be expected because the surface hydroxyl groups can capture the photoinduced holes, produce active hydroxyl radicals and prevent electron–hole recombination at the same time. The correlation presented in Fig. 10 is not linear probably because the values of OH/O_{total} ratio do not measure surface acidity. Indeed, it was reported that the surface acidity of undoped TiO_2 (anatase) and Fe-doped TiO_2 is primarily of Lewis type [82]. Thus, in agreement with previous reports [83–85], we can conclude that whereas acidity may not be the only factor which influences activity, it certainly plays an important role in the MR degradation.

Regardless of the dopant, a volcano-shaped curve was obtained for methyl red degradation against TiO_2 crystal size (Fig. 11(a)). Thus, in the cases when the samples were calcined at 700 °C, the decrease in the photocatalytic activity could be linked with the large increase of TiO_2 crystal size with an increase of calcination

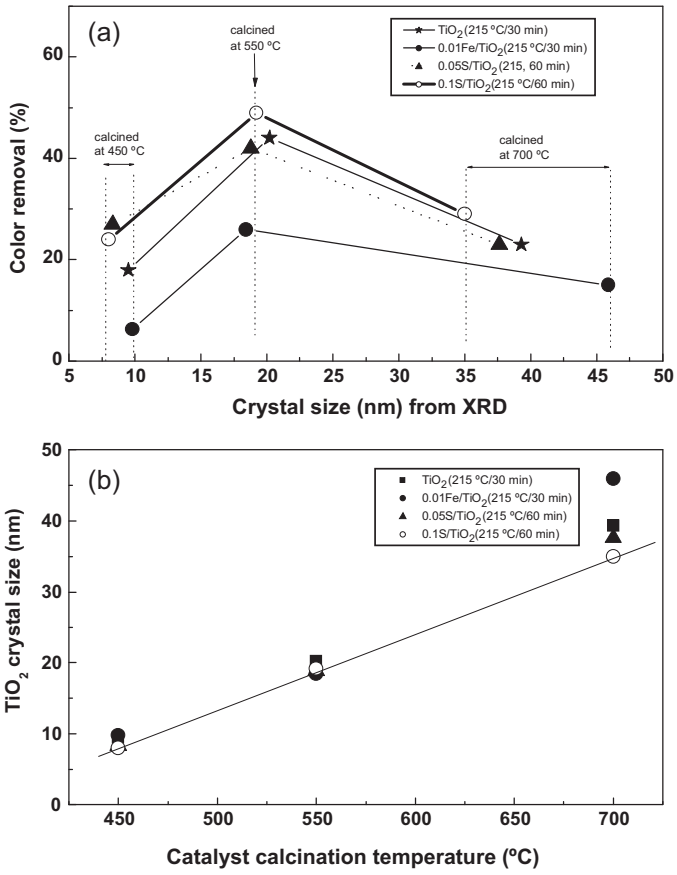

Fig. 11. (A) Influence of the TiO_2 crystal size on the photoactivity of TiO_2-based samples. (B) TiO_2 crystal size (from XRD) against calcination temperature.

temperature, as shown in Fig. 11(b). As a consequence, samples calcined at 700 °C show a lower amount of available surface active sites and a lower interfacial charge-carrier transfer rate than their counterparts calcined at 550 °C [5]. Additionally, this activity drop could be explained by the presence of undesired rutile phase (around 84% for the un-doped TiO_2 and between 37 and 40% for the *x*Fe/TiO_2 and *x*S/TiO_2, respectively). Thus, even though it is necessary to carry out a thermal treatment to the samples to obtain a photocatalytic response, the microwave assistance generates a different morphology, it is possible to reduce the effect of the calcination temperature over the presence of rutile phase and also it is possible to overcome the excessive decrease in the surface area than in the simple sol–gel synthesis method [77].

Summarizing, considering the catalyst characterization data, the largest methyl red degradation on the 0.1S/TiO_2 sample can be attributed to three factors. First, the 0.1S/TiO_2 calcined at 550 °C possesses a strong surface adsorption ability to dye molecules as was confirmed in the kinetic study. Second, this sample possesses more surface hydroxyl groups than undoped TiO_2 substrate, as deduced from TPD-NH_3 measurements (see inset of Fig. 10). Third, the crystallinity of its anatase phase is high indicating a few lattice defects and easy separation of photogenerated electrons and holes. As a consequence, the photogenerated radicals (hydroxyl and superoxide radicals) can easily react with methyl red molecules adsorbed on the catalyst surface. On the other hand, an increase of the photoactivity with an increase of S content strongly suggests that the positive effect of sulfur on the photoactivity of TiO_2 could be due to its ability to trap electrons. This process might reduce the hole–electron pair recombination at the TiO_2 surface, as it was proposed previously [31]. Finally, contrary to the S-doping, the microwave irradiation does not appear to be effective for the preparation of the *x*Fe/TiO_2 photocatalysts. A similar conclusion was obtained by Žabová and Církva [86] who reported that the preparation of Fe^{3+}-doped TiO_2 photocatalyst by microwave irradiation is detrimental for degradation of mono-chloroacetic acid and Rhodamine B under the UV irradiation.

5. Conclusions

In this work several TiO_2-based photocatalysts were prepared by a microwave-assisted synthesis methodology and tested in the methyl red dye photodegradation under UV irradiation at room temperature. By using two different dopants such as the iron and the sulfur ions to modify the TiO_2 and several temperatures and times of reaction in the microwave system and also different calcination temperatures is possible to observe the changes in surface area, crystalline phase, crystal size and band gap values of the material. Those changes could be related to the photocatalytic activity efficiency and the best material obtained by this study is the one doped at 0.1S/TiO_2 synthesized by 60 min at 215 °C in the reaction system and calcined at 550 °C reaching a 49% of color removal. A volcano-shaped curve was obtained for methyl red degradation against TiO_2 crystal size (from XRD). For the most active 0.1S/TiO_2 sample, it is inferred that S species decrease the electron–hole recombination rate. Contrary to TiO_2 doping with S^{2-} ions, the microwave synthesis is not effective for the preparation of effective *x*Fe/TiO_2 photocatalysts for the target reaction.

Acknowledgments

The authors thank to the Investigation Found of the Engineering Faculty of the UAQ (UAQ-FIFI-2011). K.E.E. also acknowledges CONACyT for a postdoctoral fellowship.

Appendix A. Supplementary data

Supplementary data associated with this article can be found, in the online version, at http://dx.doi.org/10.1016/j.apcatb.2013.03.047.

References

[1] A. Fallah Shojaie, M.H. Loghmani, Chemical Engineering Journal 157 (2010) 263–269.
[2] H.M. Yang, X.C. Zhang, Q.F. Tao, Inorganic Materials 45 (2009) 1139–1145.
[3] A. Bonamartini Corradi, F. Bondioli, B. Focher, A.M. Ferrari, C. Grippo, E. Mariani, C. Villa, Journal of the American Ceramic Society 88 (2005) 2639–2641.
[4] M. Antoniadou, V.M. Daskalaki, N. Balis, D.I. Kondarides, C. Kordulis, P. Lianos, Applied Catalysis B: Environmental 107 (2011) 188–196.
[5] X.H. Wang, J.-G. Li, H. Kamiyama, Y. Moriyoshi, T. Ishigaki, The Journal of Physical Chemistry B 110 (2006) 6804–6809.
[6] W. Choi, A. Termin, M.R. Hoffmann, Journal of Physical Chemistry 98 (1994) 13669–13679.
[7] M.A. Khan, S.I. Woo, O.-B. Yang, International Journal of Hydrogen Energy 33 (2008) 5345–5351.
[8] K. Abbas, Colloids and Surfaces A: Physicochemical and Engineering Aspects 346 (2009) 130–137.
[9] L. Kumaresan, A. Prabhu, M. Palanichamy, E. Arumugam, V. Murugesan, Journal of Hazardous Materials 186 (2011) 1183–1192.
[10] A.F. Shojaie, M.H. Loghmani, Chemical Engineering Journal 157 (2010) 263–269.
[11] V.B.R. Boppana, R.F. Lobo, Journal of Catalysis 281 (2011) 156–168.
[12] D.D. Cruz, J.C. Arévalo, G. Torres, R.G.B. Margulis, C. Ornelas, A. Aguilar-Elguézabal, Catalysis Today 166 (2011) 152–158.
[13] K. Esquivel, García F M., F. Rodríguez, M. González, L. Escobar-Alarcón, L. Ortiz-Frade, L. Godínez, Journal of Nanoparticle Research 13 (2011) 3313–3325.
[14] N. Lu, H. Zhao, J. Li, X. Quan, S. Chen, Separation and Purification Technology 62 (2008) 668–673.
[15] V.C. Papadimitriou, V.G. Stefanopoulos, M.N. Romanias, P. Papagiannakopoulos, K. Sambani, V. Tudose, G. Kiriakidis, Thin Solid Films 520 (2011) 1195–1201.
[16] T. Putta, M.-C. Lu, J. Anotai, Journal of Environmental Management 92 (2011) 2272–2276.
[17] C. Sahoo, A.K. Gupta, A. Pal, Desalination 181 (2005) 91–100.
[18] Q. Wang, S. Xu, F. Shen, Applied Surface Science 257 (2011) 7671–7677.
[19] S. Zhan, J. Yang, Y. Liu, N. Wang, J. Dai, H. Yu, X. Gao, Y. Li, Journal of Colloid and Interface Science 355 (2011) 328–333.
[20] S. Hu, F. Li, Z. Fan, C.-C. Chang, Applied Surface Science 258 (2011) 182–188.
[21] S.-I. In, P.C.K. Vesborg, B.L. Abrams, Y. Hou, I. Chorkendorff, Journal of Photochemistry and Photobiology A: Chemistry 222 (2011) 258–262.
[22] Y.-P. Peng, S.-L. Lo, H.-H. Ou, S.-W. Lai, Journal of Hazardous Materials 183 (2010) 754–758.
[23] H.-H. Ou, S.-L. Lo, C.-H. Liao, Journal of Physical Chemistry C 115 (2011) 4000–4007.
[24] S. Horikoshi, Y., Minatodani, H., Sakai, M., Abe, N. Serpone, Journal of Photochemistry and Photobiology A: Chemistry, 217 191-200.
[25] J. Yang, J. Dai, J. Li, Applied Surface Science 257 (2011) 8965–8973.
[26] Y. Wu, M. Xing, B. Tian, J. Zhang, F. Chen, Chemical Engineering Journal 162 (2011) 710–717.
[27] B. Tryba, M. Piszcz, B. Grzmil, A. Pattek-Janczyk, A.W. Morawski, Journal of Hazardous Materials 162 (2009) 111–119.
[28] P. Wang, T. Zhou, R. Wang, T.-T. Lim, Water Research 45 (2011) 5015–5026.
[29] T. Umebayashi, T. Yamaki, H. Itoh, K. Asai, Applied Physics Letters 81 (3) (2002).
[30] K. Yang, Y. Dai, B. Huang, Journal of Physical Chemistry C 111 (2007) 18985–18994.
[31] E.M. Rockafellow, L.K. Steward, W.S. Jenks, Applied Catalysis B: Environmental 91 (2009) 554–562.
[32] T. Ohno, M. Akiyoshi, T. Umebayashi, K. Asai, T. Mitsui, M. Matsumura, Applied Catalysis A – General 265 (2004) 115–121.
[33] L. Szatmáry, S. Bakardjieva, J. Subrt, P. Bezdicka, J. Jirkovsky', Z. Bastl, V. Brezovác, M. Korenkod, Catalysis Today 161 (2011) 23–28.
[34] J.A. Rengifo-Herrera, C. Pulgarin, Solar Energy 84 (2010) 37–43.
[35] V.M. Menéndez-Flores, D.W. Bahnemann, T. Ohno, Applied Catalysis B: Environmental 103 (2011) 99–108.
[36] M.R. Hoffman, S.T. Martin, W. Choi, D. Bahnemann, Chemical Reviews 95 (1995) 69–96.
[37] W.L. Gladfelter, Surface Science 605 (2011) 1146.
[38] S. Perera, E.G. Gillan, Solid State Sciences 10 (2008) 864–872.
[39] Y. Hoshi, D. Ishihara, T. Sakai, O. Kamiya, H. Lei, Vacuum 84 (2010) 1377–1380.
[40] X. Yu, Z. Shen, Vacuum 85 (2011) 1026–1031.
[41] X. Sui, Y. Chu, S. Xing, C. Liu, Materials Letters 58 (2004) 1255–1259.
[42] M. Mallak, M. Bockmeyer, P. Labmann, Thin Solid Films 515 (2007) 8072–8077.
[43] S.S. Mali, P.S. Shinde, C.A. Betty, P.N. Bhosale, W.J. Lee, P.S. Patil, Applied Surface Science 257 (2011) 9737–9746.
[44] G. Li, Y. Ding, Y. Zhang, Z. Lu, H. Sun, R. Chen, Journal of Colloid and Interface Science 363 (2011) 497–503.
[45] C.-H. Huang, Y.-T. Yang, R.-A. Doong, Microporous, Mesoporous Materials 142 (2011) 473–480.
[46] J.A. Ayllon, A.M. Peiro, L. Saadoun, E. Vigil, X. Domenech, J. Peral, Journal of Materials Chemistry 10 (2000) 1911–1914.

[47] S. Baldassari, S. Komarneni, E. Mariani, C. Villa, Materials Research Bulletin 40 (2005) 2014–2020.
[48] Y. Cao, H.-J. Wei, Z.-N. Xia, Transactions of Nonferrous Metals Society of China 19 (2009) 656–664.
[49] S. Cho, K.-H. Lee, Journal of Crystal Growth 312 (2010) 1785–1788.
[50] B. Damardji, H. Khalaf, L. Duclaux, B. David, Applied Clay Science 44 (2009) 201–205.
[51] G. Zhu, L. Pan, T. Xu, Z. Sun, Journal of Electroanalytical Chemistry 659 (2011) 205–208.
[52] N.F. Hamedani, A.R. Mahjoub, A.A. Khodadadi, Y. Mortazavi, Sensors and Actuators B: Chemical 156 (2011) 737–742.
[53] L.H. Hoang, P. Van Hai, P. Van Hanh, N.H. Hai, X.-B. Chen, I.-S. Yang, Materials Letters 65 (2011) 3047–3050.
[54] H.-E. Wang, L.-X. Zheng, C.-P. Liu, Y.-K. Liu, C.-Y. Luan, H. Cheng, Y. Yang Li, L. Martinu, J.A. Zapien, I. Bello, Journal of Physical Chemistry C 115 (2011) 10419–10425.
[55] S. Horikoshi, Y. Minatodani, H. Sakai, M. Abe, N. Serpone, Journal of Photochemistry and Photobiology A: Chemistry 217 (2011) 191–200.
[56] I. Bilecka, M. Niederberger, Nanoscale 2 (2010) 1358–1374.
[57] J.N. Hart, D. Menzies, Yi-B. Cheng, G.P. Simon, L. Spiccia, Solar Energy Materials & Solar Cells 91 (2007) 6–16.
[58] S. Komarneni, R.K. Rajha, H. Katsuki, Materials Chemistry and Physics 61 (1999) 50–54.
[59] L.H. Yang, C. Dong, J. Guo, Journal of Power Sources 175 (2008) 575–580.
[60] L. Li, X. Qin, G. Wang, L. Qi, G. Du, Z. Hu, Applied Surface Science 257 (2011) 8006–8012.
[61] P. Marcasuzaa, S. Reynaud, B. Grassl, H. Preudaomme, J. Desbriares, M. Trchova, O.F.X. Donard, Polymer 52 (2011) 33–39.
[62] Y. Shi, S. Wang, X. Ma, Chemical Engineering Journal 166 (2011) 744–750.
[63] W. Zhang, D. Li, M. Sun, Y. Shao, Z. Chen, G. Xiao, X. Fu, Journal of Solid State Chemistry 183 (2010) 2466–2474.
[64] B.S. Shirke, P.V. Korake, P.P. Hankare, S.R. Bamane, K.M. Garadkar, Journal of Materials Science: Materials Electronics 22 (2011) 821–824.
[65] Y.J. Acosta-Silva, R. Nava, V. Hernández-Morales, S.A. Macías-Sánchez, M.L. Gómez-Herrera, B. Pawelec, Applied Catalysis B: Environmental 110 (2011) 108–117.
[66] S.P. Tandon, J.P. Gupta, Physica Status Solidi (b) 38 (1970) 363–367.
[67] L. Shao, J. Chen, L. He, G. Xing, W. Lv, Z. Chen, C. Qi, Turkish Journal of Chemistry 36 (2012) 700–708.
[68] K. Esquivel, J.C. Espinosa, M.V. González, R. Guerra, L. Escobar-Alarcón, J.M. Peralta-Hernández, R. Nava, Unpublished results.
[69] Phase Identification from Powder Diffraction, USA, 2012.
[70] J. Chen, M. Yao, X. Wang, Journal of Nanoparticle Research 10 (2008) 163–171.
[71] W.-X. Xu, S. Zhu, X.-C. Fu, Q. Chen, Applied Surface Science 148 (1999) 253–262.
[72] M. Miyauchi, Journal of Materials Chemistry 18 (2008) 1858–1864.
[73] E.L.D. Hebenstreit, W. Hebenstreit, U. Diebold, Surface Science 470 (2001) 347.
[74] C.D. Wagner, W.M. Riggs, L.E. Davis, J.F. Moulder, G.E. Muilenberg, Handbook of X-ray Photoelectron Spectroscopy, Perkin-Elmer Corporation, Eden Prairie, 197876–82.
[75] L.Q. Wang, K.F. Ferris, P.X. Skiba, A.N. Shultz, D.R. Baer, M.H. Engelhard, Surface Science 440 (1999) 60–68.
[76] A. Sasahara, C.L. Pang, M. Tomitori, Journal of Physical Chemistry C 114 (2010) 20189–20194.
[77] M.A. Rauf, S.S. Ashraf, Chemical Engineering Journal 151 (2009) 10–18.
[78] A. Nageswara Rao, B. Sivasankar, V. Sadasivam, Journal of Hazardous Materials 166 (2009) 1357–1361.
[79] X. Li, P.-L. Yue, C. Kutal, New Journal of Chemistry 278 (2003) 1264–1269.
[80] A. Hoffman, E.R. Carraway, M. Hoffman, Environmental Science and Technology 28 (1994) 776–785.
[81] R. Comparelli, E. Fanizza, M.L. Curri, P.D. Cozzoli, G. Mascolo, R. Passino, A. Agostiano, Applied Catalysis B: Environmental 55 (2005) 81–91.
[82] C. Monterra, Journal of the Chemical Society, Faraday Transactions 1: Physical Chemistry in Condensed Phases 84 (1988) 1617–1637.
[83] T. Yamaguchi, Y. Tanaka, K. Tanabe, Journal of Catalysis 65 (1980) 442–447.
[84] K. Tanabe, M. Misono, Y. Ono, H. Hattori, New Solid Acids and Bases: Their Catalytic properties, Elsevier Science Publishers, New York, 1989.
[85] J. Papp, S. Soled, K. Dwight, A. Wold, Chemistry of Materials 6 (1994) 496–500.
[86] H. Žabová, V. Církva, Journal of Chemical Technology and Biotechnology 84 (11) (2009) 1624–1630.